

Short-term dynamics of a density interface following an impact

A. ANTKOWIAK, N. BREMOND, S. LE DIZÈS
AND E. VILLERMAUX†

IRPHÉ, Aix–Marseille Université, CNRS, Technopôle de Château-Gombert 49, rue Frédéric Joliot-Curie 13384 Marseille Cedex 13, France

(Received 16 November 2006 and in revised form 22 January 2007)

A tube filled with a perfectly wetting liquid falls axially under its own weight. In its gravity-free reference frame, the liquid interface is deformed by surface tension into a hemispherical shape. On impact of the tube on a rigid floor, the interface curvature reverses violently, forming a concentrated jet. If the contact angle at the tube wall is such that the interface is flat, the liquid rebounds as a whole with the tube, with no deformation. We analyse this phenomenon using an impulse pressure description, providing an exact description of the initial liquid velocity field at the impact, supported by high-speed image velocimetry measurements. This initial dynamics is insensitive to liquid surface tension and viscosity.

1. Introduction

Liquid jets, or ligaments, are the sinews of atomization (Villermaux 2007) as drops always result from the rupture of more or less smooth threads. Ubiquitous features of free-surface flows, jets naturally erupt in a wide variety of situations, including bursting bubbles (Blanchard 1967), overdriven Faraday waves (Longuet-Higgins 1983) or collapsing voids (Benjamin & Ellis 1966) as classical examples. Another common occurrence of jet formation is the one resulting from an impact, illustrated on figure 1 with the paradigmatic experiment referred to as ‘Pokrovski’s experiment’ in Lavrentiev & Chabat (1980): a glass tube filled with water falls axially under its own weight. In its gravity-free reference frame, the liquid interface deforms by surface tension into a close-to-hemispherical shape (meniscus) to adapt to the wetting condition at the wall. On the impact of the tube on a rigid floor, the interface curvature reverses violently, forming a concentrated jet. Interestingly, when the tube wall is altered such that the contact angle is around 90° , the interface is initially flat, and not deformed after rebound (figure 2). This simple experiment shows the crucial role of the free-surface geometry on its later evolution. This important effect has been known for more than a century in the context of ‘shaped-charge jets’ (Birkhoff *et al.* 1948). Military devices exploiting this effect basically consist of lining an explosive charge with an artificial ‘meniscus’ made of metal that collapses with the detonation wave and produces an intense metallic liquid jet. Whereas the resulting jet velocity typically scales with the detonation wave celerity (of order of several kilometres per second), the jet produced here with the impacting tube scales with the impact velocity, suggesting a different mechanism of jet formation.

† Also at: Institut Universitaire de France.

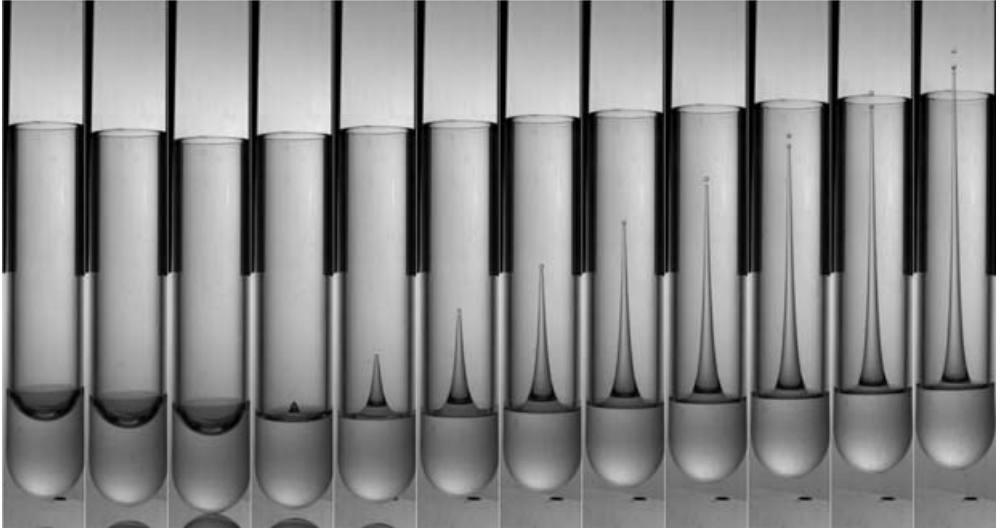


FIGURE 1. A tube filled with a wetting liquid and falling under gravity gives rise to a strong jet after impact. The interval separating each snapshot of this sequence is 5.5 ms.

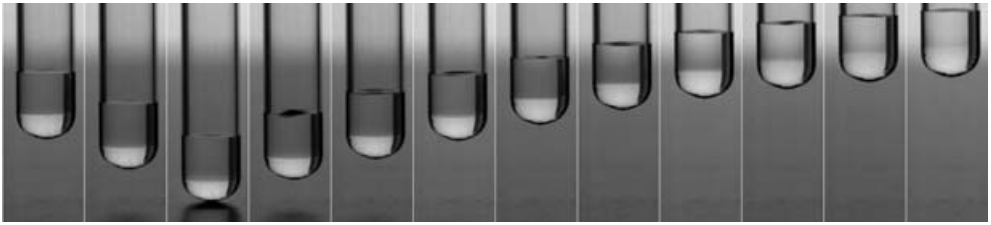


FIGURE 2. When the tube wall is made hydrophobic (silanization), the interface is initially flat, and not deformed after rebound.



FIGURE 3. A liquid with a free surface is falling as a whole under gravity. A bubble at the free surface gives rise to a strong jet after impact. The interval separating each snapshot of this sequence is 1 ms.

The purpose of the study is to elucidate the role of free-surface corrugations, not only associated with menisci, but also with standing waves or bubbles cavities (see figure 3) in the initial interface dynamics. We proceed as follows: in §2, employing a pressure impulse approach (Batchelor 1967; Cooker & Peregrine 1995), the pressure field associated with impact as well as the corresponding velocity field are derived using a variant of the multipole expansion. In §3, the theoretical results are compared to measurements of the liquid displacement field using high-speed video and particle

image velocimetry (PIV). The roles of confinement, surface tension (including the case of non-cohesive fluids) and viscosity are discussed finally.

2. Pressure impulse in an impacted tube

A sudden change in the tube velocity induces pressure gradients which in turn produce a sudden change in the liquid velocity (Batchelor 1967, § 6.10). Looking more closely at the very short time dynamics, the impact pressure field is established via a complex acoustic field radiated from the boundaries. Typically, these phenomena occur on a few acoustic time scales corresponding to what we call the impact duration τ (here, τ is observed to be 10^{-4} s, whereas the acoustic time scale is 10^{-5} s). Over the impact period, neither the velocity nor its spatial gradients are expected to balance the dominant time derivative, such that the dynamics is assumed to be governed by

$$\frac{\partial \mathbf{u}}{\partial t} = -\frac{1}{\rho} \nabla p. \tag{2.1}$$

As is common in impact studies (Cooker & Peregrine 1995), the details of the acoustic field are not examined and an incompressible evolution ruled by global momentum balances is considered, just as in the problem of billiard ball impact where the elastic wave field is classically neglected. On integrating (2.1) over the impact duration, the velocity field after impact is found:

$$\mathbf{u}(\tau) - \mathbf{u}(0) = -\frac{1}{\rho} \nabla P, \tag{2.2}$$

where P is the *impulse pressure* defined by

$$P = \int_0^\tau p \, dt, \tag{2.3}$$

accounting for the total liquid pressure variation associated with impact (or impulse gravity). Incompressibility implies that P is an harmonic function:

$$\Delta P = 0. \tag{2.4}$$

Note that the neglected viscous terms are identically nil, the velocity field being the gradient of an harmonic potential. Consequently, there are no viscous effects in the volume, and the region of influence of viscosity is concentrated near the free surface and the wall in a thin boundary layer of thickness $\sqrt{\nu\tau}$, with ν the kinematic viscosity.

The purpose of the following development is to derive the solution of the Laplace equation (2.4) for the physical set-up sketched in figure 4. It consists of an infinite vertical tube of radius R/λ filled with liquid. At the free surface, a bubble of radius R ($\leq R/\lambda$, so that the ‘confinement factor’ λ lies in the range $0 < \lambda \leq 1$), modelled with an hemisphere, is present. At initial time, the container is impulsively started, with a velocity $U_0 \mathbf{e}_z$. The associated impulse pressure satisfies $P = 0$ at the free surface. On the solid boundaries, the boundary conditions derive from (2.2):

$$U_n = -\frac{1}{\rho} \frac{\partial P}{\partial n}, \tag{2.5}$$

where $U_n = U_0(\mathbf{e}_z \cdot \mathbf{n})$. At the infinitely deep bottom, the impact enforces $\partial P / \partial z = -\rho U_0$.

Were no bubble present, the trivial solution $-\rho U_0 z$ would hold for the impulse pressure field. This ‘impulsive hydrostatic’ pressure distribution imparts an equal momentum distribution within the liquid bulk. Each fluid particle acquires a

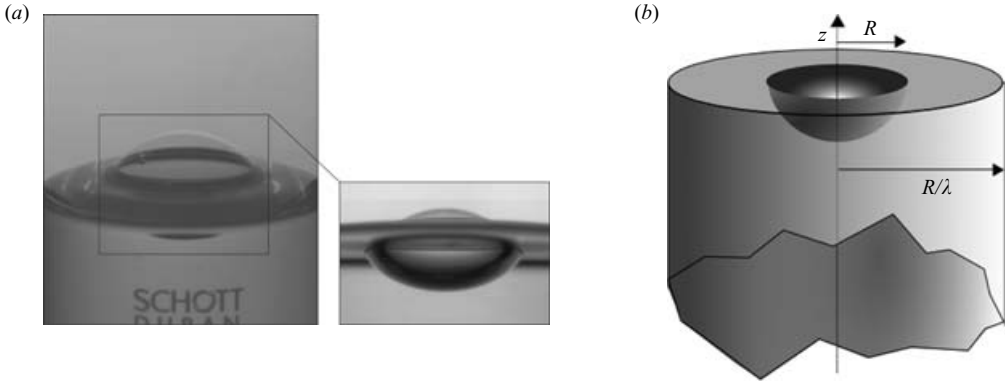


FIGURE 4. (a) Typical experiment showing a cavity produced with a bubble, just before impact. (b) Sketch of the liquid domain in the theoretical idealization.

velocity $U_0 e_z$ after impact in the fixed frame, that is zero velocity in the moving frame: incompressibility guarantees that the sudden change in the container velocity is instantaneously transmitted to all fluid particles through the pressure linear stratification. This instructive example, illustrated in figure 2, shows that the only free-surface geometry compatible with the preceding impulsive hydrostatic pressure distribution is a planar one; enforcing a zero pressure distribution on a curved surface will generate corrections to the pressure field. This is the situation under study: free-surface corrugations, possibly produced with the help of surface tension, but not exclusively, will give rise to pressure and velocity corrections.

Analytically, solutions of the Laplace equation are easily found when the boundaries of the domain are iso-coordinate surfaces. Conversely, the present problem is ‘hybrid’ in this sense as the boundaries are iso-coordinates of two representation systems. Knight (1936) made a first step in building solutions to such ‘mixed’ problems, considering a problem with an identical geometry. Closely following the original treatment of Knight, we shall now investigate and solve the pressure impulse problem.

2.1. Elementary harmonic solutions in the cylindro-spherical domain: modified multipoles

In the following, each field considered will have two representations: cylindrical (ξ, Φ, z) and spherical (r, θ, Φ) . With these two views, it is possible to express the requirements on the general solution F to the present problem:

$$\left. \begin{array}{l} \text{(i)} \quad \Delta F = 0 \text{ in the whole domain } (r \geq R, \xi \leq R/\lambda, z \leq 0), \\ \text{(ii)} \quad \partial F / \partial \xi = 0 \text{ on the cylinder surface } \xi = R/\lambda, \\ \text{(iii)} \quad F = 0 \text{ on the plane } z = 0, \\ \text{(iv)} \quad F = 0 \text{ on the sphere surface } r = R. \end{array} \right\} \quad (2.6)$$

Without condition (ii), expressing the impermeability condition on the cylinder, a standard approach would consist of an expansion of the solution into odd multipoles (each readily satisfying (i) and (iii)) so as to meet condition (iv) on the sphere. With the cylinder included, the strategy remains similar, but the base functions are modified with the help of regular cylindrical harmonic functions in order to satisfy (ii).

2.1.1. *The modified dipole*

The dipolar field $\phi(r, \theta) = -\partial r^{-1}/\partial z = \cos \theta/r^2$, which is a singular solution to the Laplace equation in spherical coordinates, fails to meet condition (ii) as already noticed. It is therefore desirable to build a solution of the form $F_0 = \phi(r, \theta) + \varphi(\xi, z)$, where $\varphi(\xi, z)$ is a regular solution to the Laplace equation in cylindrical coordinates preserving (i) and (iii) but derived so that F_0 complies with (ii). Regularity and symmetry requirements suggest the following form for φ :

$$\varphi(\xi, z) = \int_0^\infty f(m) \sin(mz) I_0(m\xi) dm, \tag{2.7}$$

where the spectral decomposition $f(m)$ is unknown for the moment. On the cylinder surface, the derivatives with respect to ξ of the regular and singular parts must balance each other:

$$-\frac{\partial \phi}{\partial \xi}(R/\lambda, z) = 3 \frac{(R/\lambda)z}{((R/\lambda)^2 + z^2)^{5/2}} = \frac{\partial \varphi}{\partial \xi}(R/\lambda, z) = \int_0^\infty m f(m) \sin(mz) I_1(mR/\lambda) dm. \tag{2.8}$$

Inverting the sine Fourier transform provides the expression for the spectral amplitude:

$$f(m) = \frac{2}{\pi} \int_{-\infty}^0 \frac{\sin(mz)}{m I_1(mR/\lambda)} \left\{ 3 \frac{(R/\lambda)z}{((R/\lambda)^2 + z^2)^{5/2}} \right\} dz. \tag{2.9}$$

This spectral decomposition allows the expression for $\varphi(\xi, z)$ to be recovered:

$$\varphi(\xi, z) = \frac{2}{\pi} \int_0^\infty m \frac{K_1(mR/\lambda)}{I_1(mR/\lambda)} \sin(mz) I_0(m\xi) dm, \tag{2.10}$$

where the following relation has been used:

$$\int_{-\infty}^0 \frac{az \sin(mz)}{(a^2 + z^2)^{5/2}} dz = \frac{1}{3} m^2 K_1(ma). \tag{2.11}$$

Relation (2.10) explicits the correction to the dipolar field needed so that the resulting modified dipole F_0 satisfies (i), (ii) and (iii).

Although exact, (2.10) does not appear to have the most relevant form in view of the formulation of condition (iv) on the sphere. A more appropriate form in the vicinity of the sphere consists of a zonal harmonics expansion. Using the following identity (Knight 1936):

$$\sin(mz) I_0(m\xi) = \sum_{n=0}^\infty (-1)^n \frac{m^{2n+1} r^{2n+1}}{(2n+1)!} P_{2n+1}(\cos \theta), \tag{2.12}$$

where $P_{2n+1}(\cos \theta)$ is the Legendre polynomial of degree $2n + 1$, one can also obtain the following expression for the modified dipole:

$$F_0(r, \theta) = \left(\frac{R}{r}\right)^2 \cos \theta + \sum_{n=0}^\infty \lambda^{2n+3} \alpha_{2n+1}^{(0)} \left(\frac{r}{R}\right)^{2n+1} P_{2n+1}(\cos \theta), \tag{2.13}$$

with

$$\alpha_{2n+1}^{(0)} = \frac{(-1)^n}{(2n+1)!} \frac{2}{\pi} \int_0^\infty m^{2n+2} \frac{K_1(m)}{I_1(m)} dm. \tag{2.14}$$

2.1.2. Modified multipoles

As remarked by Knight, differentiating F_0 with respect to z an even number of times gives functions sharing analogous properties, namely harmonicity (i), boundary condition (ii) as well as condition (iii). Upon recalling that

$$-\frac{\partial^{2s+1}}{\partial z^{2s+1}} \left(\frac{1}{r} \right) = \frac{\partial^{2s}}{\partial z^{2s}} \left(\frac{\cos \theta}{r^2} \right) = (2s + 1)! \frac{P_{2s+1}(\cos \theta)}{r^{2s+2}}, \tag{2.15}$$

$$\frac{1}{(2s)!} \frac{\partial^{2s}}{\partial z^{2s}} \sum_{n=0}^{\infty} r^{2n+1} P_{2n+1}(\cos \theta) = \sum_{n=0}^{\infty} C_{2n+2s+1}^{2s} r^{2n+1} P_{2n+1}(\cos \theta), \tag{2.16}$$

where $C_{2n+2s+1}^{2s}$ are binomial coefficients, these solutions can be written

$$\begin{aligned} F_{2s} &= \frac{R^{2s}}{(2s)!} \frac{\partial^{2s} F_0}{\partial z^{2s}} \\ &= (2s + 1) \left(\frac{R}{r} \right)^{2s+2} P_{2s+1}(\cos \theta) + \sum_{n=0}^{\infty} \lambda^{2n+2s+3} \alpha_{2n+1}^{(2s)} \left(\frac{r}{R} \right)^{2n+1} P_{2n+1}(\cos \theta) \end{aligned}$$

where

$$\alpha_{2n+1}^{(2s)} = C_{2n+2s+1}^{2s} \alpha_{2n+2s+1}^{(0)}. \tag{2.17}$$

2.2. Formal expansion of the complete solution

Having derived the modified multipoles, it is natural to seek the complete solution in an expansion of the form $P = \sum_0^\infty A_{2s} F_{2s}$. However, since the functions F_{2s} are expected to decrease asymptotically to 0 for large z as F_0 , it appears difficult to comply with the additional constraint $\lim_{z \rightarrow -\infty} \partial P / \partial z = -\rho U_0$. While the suggested expansion is natural in the context of a decaying electrostatic potential field created with a charged sphere (the original context of Knight), here it fails to capture the solution; elementary solutions of the Laplace equation linear in Cartesian variables cannot be expressed as a convergent series of modified multipoles and have therefore to be included separately. More specifically, the ‘impulsional hydrostatic’ pressure field $-\rho U_0 z$ evoked earlier has to be added to the complete solution:

$$P(r, \theta) = -\left(\frac{r}{R} \right) P_1(\cos \theta) + \sum_{s=0}^{\infty} A_{2s} F_{2s}, \tag{2.18}$$

with P here expressed in units of $\rho U_0 R$.

In the case of a charged sphere, the potential is forced through inhomogeneous boundary conditions on the sphere surface. Conversely, the impact induces a linear pressure profile, incompatible with pressure cancellation on the (non-planar) free surface. The impact therefore drives in return the emergence of a multipolar field.

Having included this forcing, the linear relationship between the coefficients of the expansion derives from the constraint of vanishing pressure on the bubble surface. Once projected on each Legendre polynomial $P_{2n+1}(\cos \theta)$, this is

$$(2n + 1) A_{2n} + \sum_{s=0}^{\infty} \lambda^{2n+2s+3} \alpha_{2n+1}^{(2s)} A_{2s} = \delta_{0n}. \tag{2.19}$$

In the case of weak confinement (e.g. an isolated bubble), the first-order approximation of these coefficients is

$$A_0 = 1 - \lambda^3 \alpha_1^{(0)}, \quad A_{2n} = -\lambda^{2n+3} \alpha_{2n+1}^{(0)} / (2n + 1), \tag{2.20}$$

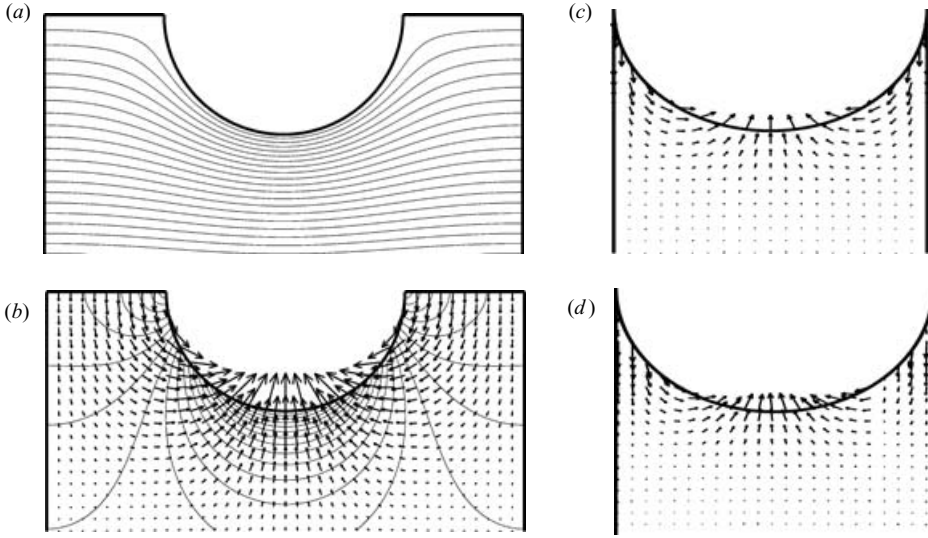


FIGURE 5. (a) Pressure levels and (b) velocity field obtained with the cylindrical representation for confinement factor $\lambda = 0.5$. (a) Isobars are equispaced with a step of $0.08\rho U_0 R$. (b) Velocity vectors and levels of the pressure gradient norm equispaced with a step of $0.12\rho U_0$. (c) The theoretical velocity field for the confined geometry ($\lambda = 1$) and (d) a typical velocity field obtained experimentally after PIV treatment.

revealing the dominance of the dipolar field in the correction for a large range of confinements. But in the general case where confinement cannot be introduced perturbatively, the solution of system (2.19) can still be obtained by numerical means, after truncation at a suitable order. In all cases, inclusion of ten modified multipoles appears sufficient to guarantee the respect of condition (iv) with an absolute error less than 10^{-4} .

Finally, given the general expression for the impulse pressure (2.18), and with the help of the governing equation (2.1), the liquid velocity field in a frame moving with the container is

$$\mathbf{u}(r, \theta) = -U_0 R \nabla \left(\sum_{s=0}^{\infty} A_{2s} F_{2s} \right). \quad (2.21)$$

Figure 5 illustrates typical pressure impulse distributions for different confinement factors. The strong inhomogeneity of the pressure gradient field is remarkable and entirely induced by the corrugation of the free surface (driving the emergence of multipoles through condition (iv)). Immediately after impact, the strongly inhomogeneous pressure field induced by the impact is converted into a similarly inhomogeneous kinetic energy distribution, through the governing equation (2.1). The corresponding velocity fields are represented in figure 5(b, c).

From the above analysis, the following physical picture emerges: introducing a free-surface corrugation of, say, depth H and typical curvature radius R induces a deformation of the isobars surrounding the cavity, as illustrated in figure 5(a). The isobar squeeze is then naturally reflected in the pressure gradient intensity in the vicinity of the cavity bottom. Taking the pressure level at the cavity depth far from the corrugation, i.e. $\rho U_0 H$, and the natural length scale of the cavity, i.e. R , as characteristic scales, the order of magnitude of the pressure gradient is expected to be

$$\frac{\partial P}{\partial z} \approx -\rho U_0 \frac{H}{R}. \quad (2.22)$$

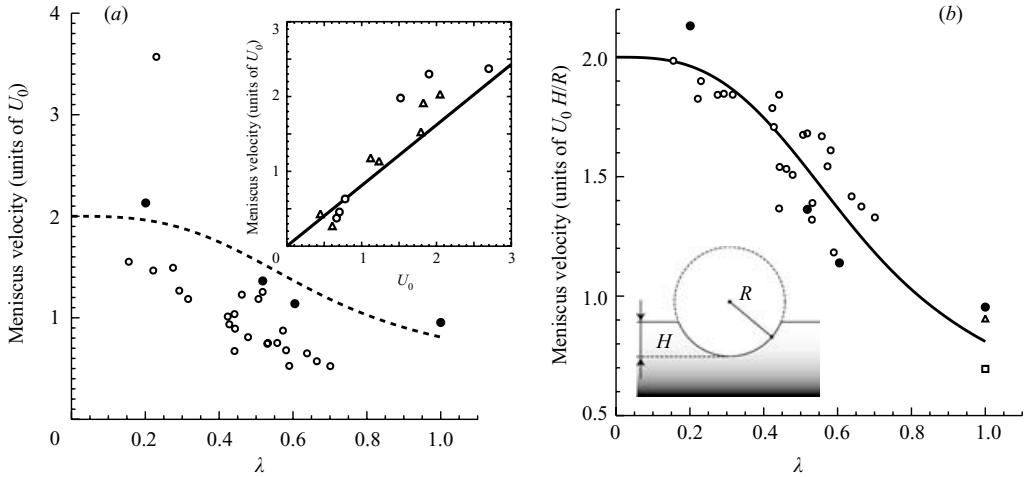


FIGURE 6. (a) Maximum meniscus velocity at the impact in a frame moving with the container in units of U_0 , as a function of the confinement factor λ . The dotted line corresponds to the theoretical prediction, and the circles to the experimental observation (filled circles correspond to near hemispherical bubbles, $H/R \sim 1$). The inset illustrates the linear dependence between the meniscus velocity and the impact velocity in the confined ($\lambda = 1$) case for two tubes (\circ , glass bottom; \triangle , aluminium bottom). (b) As (a), but rescaled with the aspect ratio H/R of the bubble. Water is the working fluid; \triangle , an experiment with ethanol (of surface tension 3 times smaller than water); \square , an experiment conducted with V50 silicon oil of dynamic viscosity 50 times larger than water.

Although H and R are basically the same quantity in the theoretical idealization, this scale distinction will prove useful in the analysis of the experimental results.

3. Experiments and comparisons

Experiments have been conducted using a high-speed Photron video camera at typically 3000 frames per second at a resolution of 1024×1024 pixels. Theory predicts a decrease of the initial meniscus maximal velocity (on the tube axis) as the confinement factor λ tends to 1. This behaviour, already visible from a comparison of the velocity fields plotted in figures 5(c) and 5(b), is detailed in figure 6. In a frame moving with the container, the initial velocity at the cavity bottom is reported for different confinement ratios and compared with the theoretical prediction. The agreement is correct only for near-hemispherical bubbles having comparable curvature radius and cavity depth. Our theory does not consider cavities such that $H/R \neq 1$ (with H and R defined figure 6b). But the mechanism described below equation (2.21) anticipates a linear dependence of the cavity velocity with H/R . And dividing all the observed velocities by this geometrical quantity leads to a better agreement between theory and experiments (figure 6b).

The structure and intensity of the velocity field was measured using PIV at the moment of impact in the confined geometry ($\lambda = 1$) by seeding the liquid (water) with $100 \mu\text{m}$ particles. A vertical plane containing the tube symmetry axis was illuminated with a laser sheet produced by a continuous 2 W Argon laser. Classical PIV treatment (Meunier & Leweke 2003) gives access to the bulk velocity field. A typical result is shown figure 5(d), in qualitative agreement with the theoretical velocity field (figure 5c). Quantitative comparison is provided by examining the radial and axial velocity profiles along a horizontal line tangent to the meniscus, and the tube axis of symmetry as shown on figure 7. This quantitative agreement is achieved

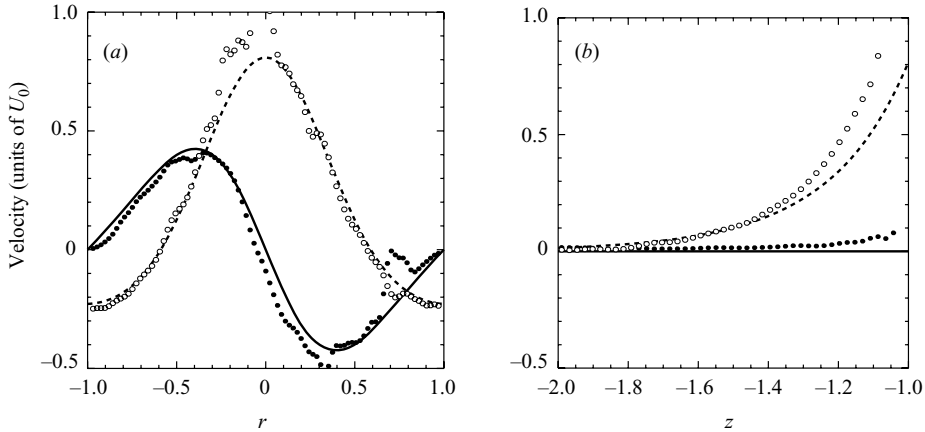


FIGURE 7. Comparison between theoretical and experimental velocity profiles, in units of U_0 in the confined geometry ($\lambda = 1$); (a) along a ray tangent to the meniscus; (b) along the symmetry axis. The thick (dotted) line correspond to the radial (axial) theoretical velocity. The filled (open) circles represent an experimental observation with water, in a 3 cm diameter glass tube. The impact velocity is 6 m s^{-1} .

within a purely inertial theory accounting for the deformation of the hydrostatic impulse pressure field by the presence of the cavity, disregarding viscous and surface tension stresses. In particular, the viscous boundary layer at the tube wall is not seen (figure 7a).

4. Conclusions and extension to non-cohesive fluids

The early time deformation of a curved density interface following an impact has been elucidated. An impact induces an impulsional linear pressure stratification within the bulk, transmitting the information from the sudden velocity change to all fluid particles. For the fluid to move as a whole, the free surface has to be planar. Any departure from the plane will induce impulse pressure corrections, and hence motions within the bulk. This resulting velocity field has been derived analytically for free-surface corrugations ranging from isolated bubbles to menisci by means of a purely inertial theory, in agreement with experimental observations. Viscous effects do not appear to be relevant in the present problem (no visible effect associated with viscous boundary layers nor deviation of the cavity velocity with an oil 50 times more viscous than water), consistently with our description.

Interestingly, the free-surface corrugations considered experimentally could not have been produced without the help of surface tension since it is necessary in the formation of menisci, or bubbles. But the dynamics subsequent to the impact does not rely on surface tension. Further proof of the insensitivity to surface tension is obtained by considering a non-cohesive deformable medium, namely sand, as working fluid. A first experiment consists of observing the impact of a tube filled with sand with a planar free surface (figure 8). Here, no jet is observed and the sand particles are at best superficially fluidized. In a second experiment, an artificial ‘meniscus’ is sculpted at the free surface and a strong jet is observed just after the impact, like that observed after the impact of a sphere on sand bed (Thoroddsen & Shen 2001). The non-cohesive character of the medium certainly confirms surface tension as irrelevant in the present experiment. Moreover, the fact that a jet emerges in that case too

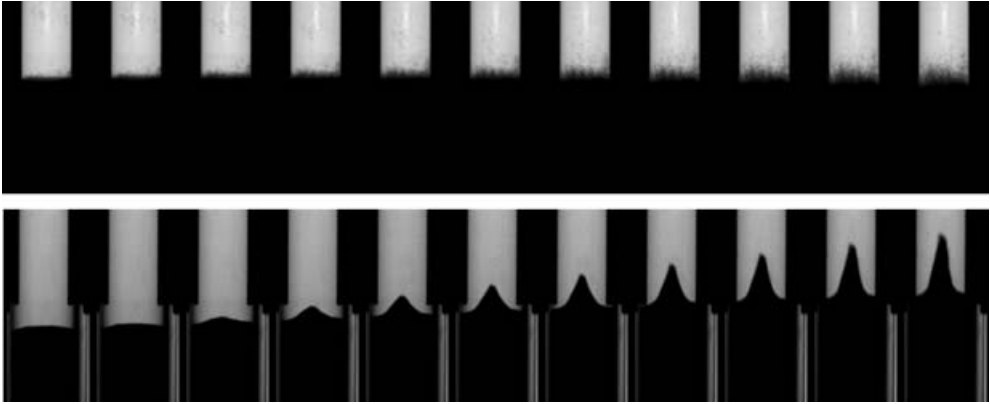


FIGURE 8. Top: a tube filled with sand with a flat surface impacts. 2 ms separates each snapshot of the sequence. Bottom: the same tube with a sculpted ‘meniscus’ impacts. There is a time interval of 1 ms between each image.

pinpoints the universal/ubiquitous aspect of jet formation in a medium with a curved stress-free surface and initial harmonic pressure (or stress) distribution.

The subsequent development of the free surface, which rapidly evolves both in shape and velocity, is therefore expected to be insensitive to surface tension and viscosity. The features of the resulting stretched jet, the regions and time scales over which viscosity and surface tension will eventually come into play and the ultimate fragmentation of the jet into droplets are currently under investigation.

This work was supported by the Agence Nationale de la Recherche through grant ANR05-BLAN-0222-01, and by EADS Foundation.

REFERENCES

- BATCHELOR, G. K. 1967 *An Introduction to Fluid Dynamics*. Cambridge University Press.
- BENJAMIN, T. B. & ELLIS, A. T. 1966 A discussion on deformation of solids by the impact of liquids, and its relation to rain damage in aircraft and missiles, to blade erosion in steam turbines, and to cavitation erosion. *Phil. Trans. R. Soc. Lond. A* **260**, 221–240.
- BIRKHOFF, G., MACDOUGALL, D. P., PUGH, E. M. & TAYLOR, G. I. 1948 Explosives with lined cavities. *J. Appl. Phys.* **19**, 563–582.
- BLANCHARD, D. C. 1967 *From Raindrops to Volcanoes*. Doubleday, re-edited by Dover in 2004.
- COOKER, M. J. & PEREGRINE, D. H. 1995 Pressure-impulse theory for liquid impact problems. *J. Fluid Mech.* **297**, 193–214.
- KNIGHT, R. C. 1936 The potential of a sphere inside an infinite circular cylinder. *Q. J. Maths. (Oxford series)* **7**, 124–133.
- LAURENTIEV, M. & CHABAT, B. 1980 *Effets Hydrodynamiques et Modèles Mathématiques*. Éditions MIR, translated from the 1977 Russian edition.
- LONGUET-HIGGINS, M. S. 1983 Bubbles, breaking waves and hyperbolic jets at a free surface. *J. Fluid Mech.* **127**, 103–121.
- MEUNIER, P. & LEWEKE, T. 2003 Analysis and treatments of errors due to high velocity gradients in particle image velocimetry. *Exps. Fluids* **35**, 408–421.
- THORODDSEN, S. T. & SHEN, A. Q. 2001 Granular jets. *Phys. Fluids* **13**, 4–6.
- VILLERMAUX, E. 2007 Fragmentation. *Annu. Rev. Fluid Mech.* **39**, 419–446.